

Revealing Charge Transfer in Defect-Engineered $4H_b$ -TaS₂

Siavash Karbasizadeh,^{1,2,*} Woojin Yang,^{2,3} Wonhee Ko,^{3,4}
Haidong Zhou,³ An-Ping Li,² Tom Berlijn,^{2,†} and Sai Mu^{1,‡}

¹*SmartState Center for Experimental Nanoscale Physics, Department of Physics and Astronomy,
University of South Carolina, Columbia, SC, 29208, USA*

²*Center for Nanophase Materials Science, Oak Ridge National Laboratory, Oak Ridge, Tennessee 37831, USA*

³*Department of Physics and Astronomy, University of Tennessee, Knoxville, Tennessee 37996, USA*

⁴*Center for Advanced Materials and Manufacturing,
University of Tennessee, Knoxville, Tennessee 37920, USA*

(Dated: March 26, 2026)

We present a comprehensive first-principles investigation of defects in $4H_b$ -TaS₂. In this layered transition metal dichalcogenide, charge transfer between alternating Mott-insulating 1T and metallic 1H layers gives rise to exotic quantum phases such as the Kondo effect and topological superconductivity. Motivated by recent defect manipulation in $4H_b$ -TaS₂ via STM, we address their microscopic nature and impact on interlayer charge transfer. To this end, we systematically analyze over 90 defects using large-scale density functional theory (DFT) calculations. Our extensive dataset, compiled from STM simulations, defect formation energies, work functions, and charge transfer, establishes a foundational resource for future theoretical and experimental studies on defect engineering in $4H_b$ -TaS₂.

I. INTRODUCTION

Transition metal dichalcogenide $4H_b$ -TaS₂ is a two-dimensional layered material that consists of alternating layers of 1T-TaS₂ and 1H-TaS₂ (see Fig. 1(a)). In bulk 1T-TaS₂, the monolayer layers represent a half-filled Mott insulator and a candidate quantum spin liquid[1]. In this layer, clusters of 13 Ta atoms reorganize into a Star-of-David (SoD) configuration, as seen in Fig. 1(b). The Ta atoms move toward the cluster center, leaving one localized electron on the central Ta atom. This results in localized spins on a triangular lattice, characteristic of the half-filled Mott insulating state [1–9]. In contrast, bulk 2H-TaS₂, whose layers are equivalent to the 1H layers in $4H_b$ -TaS₂, is metallic and becomes a strongly spin-orbit coupled superconductor at $T_c = 3.4$ K [10–15]. Combining 1T and 1H polytypes into $4H_b$ -TaS₂ offers a rich platform to investigate strongly correlated and topological effects. In this heterostructure, coupling between the localized moments of the 1T layer and the itinerant electrons of the 1H layer significantly modifies the physics of both constituents. The charge transfer depletes the 1T flat band and converts the localized spins into a Kondo lattice, while doping and inversion symmetry breaking in the 1H layers modify the superconducting state into a nodal topological superconductor [16–29]. Scanning tunneling microscopy and transport measurements reveal quasi-periodic one-dimensional modulations and a two-fold symmetric superconducting critical field characteristic of a multiple-component nematic superconducting order parameter [30]. The superconductivity in

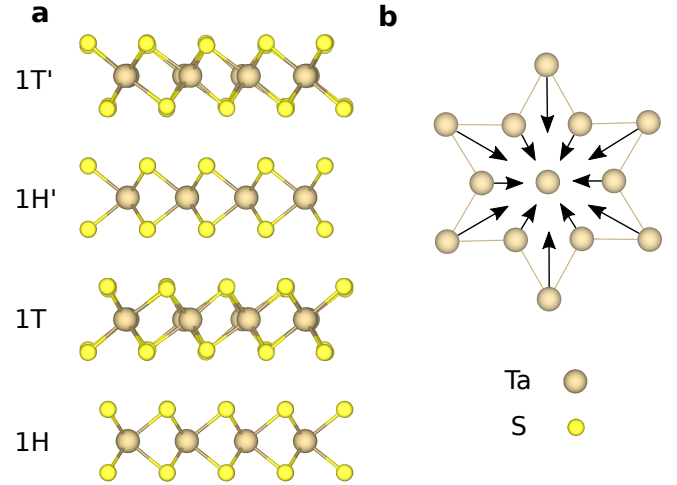


FIG. 1. (a) Bulk $4H_b$ -TaS₂ structure from the side. Brown spheres show tantalum, while the yellow spheres show sulfur. (b) Tantalum atoms constructing the star of David. Black arrows show the displacements of the charge density wave distortion.

$4H_b$ -TaS₂ is further marked by edge modes and zero-bias conductance peaks at vortex cores consistent with Majorana bound states [31], suggesting relevance for quantum memory and quantum computing. These observations emphasize the crucial role of charge transfer in transforming the Mott-derived localized spins into a Kondo lattice and in enabling the unconventional and topological superconductivity observed in $4H_b$ -TaS₂.

In our recent study [32], we demonstrated that charge transfer in $4H_b$ -TaS₂ can be further tuned locally through the manipulation of individual defects. In that work, two distinct types of defects were identified, referred to as type 1 and type 2, which can also be visually recognized in earlier scanning tunneling microscopy (STM)

* siavashk@email.sc.edu

† berlijn@ornl.gov

‡ mus@mailbox.sc.edu

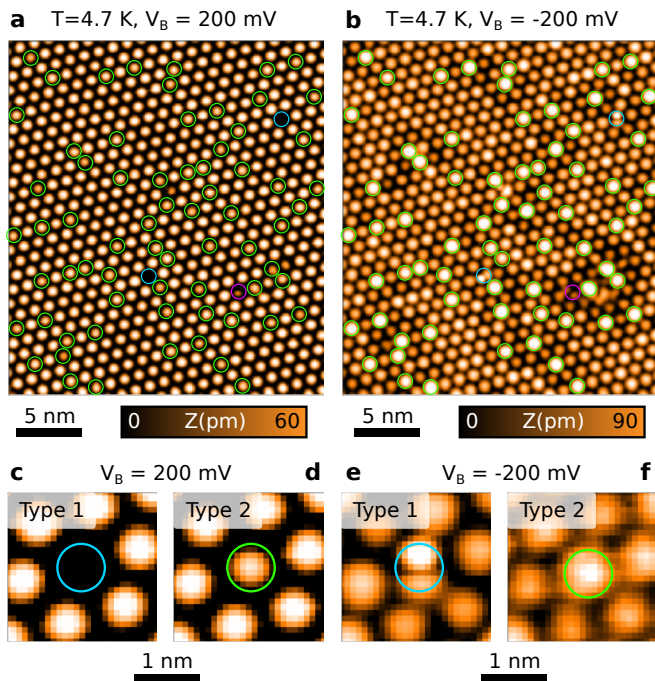


FIG. 2. Scanning tunneling microscopy (STM) image of 1T-terminated $4H_b$ -TaS₂ at V_{bias} of (a) 200 mV, and (b) -200 mV. Types 1 and 2 defects are specified using cyan and neon green circles. Both images were measured at a tunneling current of 10 pA. Parts (c)-(f) show magnified images of the defects in both positive and negative biases. We have also used a purple circle to show a different type of defect that does not belong in the type 1 or 2 categories.

data [16]. In the present manuscript, STM images illustrating these two defect types are shown in Fig. 2(a) and (b), acquired on a 1T-terminated surface. In these images, each bright spot corresponds to a Star-of-David (SoD) cluster, with the bright peak at the cluster center originating from the inward displacement of atoms, as illustrated in Fig. 1(b). Type 1 defects do not display the central SoD peak at positive bias [see Fig. 2(c)], whereas type 2 defects retain the SoD peak at positive bias and follow the symmetric SoD pattern, with slightly reduced intensity relative to pristine SoDs, as shown in Fig. 2(d). At negative bias, type 1 defects exhibit pronounced asymmetry, characterized by an off-centered peak and/or loss of threefold symmetry [Fig. 2(e)], while type 2 defects show strongly enhanced SoD peak intensity compared to pristine CDW regions [Fig. 2(f)]. Beyond characterization, STM was also used to reversibly create and remove type 1 defects, enabling local control of charge transfer and providing a pathway to manipulate the emergent properties of $4H_b$ -TaS₂.

To understand the microscopic origin of the defects shown in Fig. 2, we previously interpreted them as sulfur vacancies [32]. Specifically, type 1 defects were proposed to correspond to sulfur vacancies in the 1T layer, and type 2 defects to sulfur vacancies in the 1H layer. These assignments are supported by STM simulations and lo-

cal density of states calculations in that work. While the assignment of type 1 defects to sulfur vacancies is further supported by their ease of STM manipulation, an intriguing observation in the STM data remains unresolved: type 2 defects appear far more frequently than type 1, as seen in previous studies [16, 32] and in our Fig. 2. The higher prevalence of type 2 defects suggests they may differ in nature, or that a mechanism must be identified to explain their abundance. Furthermore, our STM measurements in Ref. [32] revealed that type 1 and type 2 defects qualitatively influence charge transfer between the layers. However, STM primarily resolves lateral spatial variations and can probe only one layer at a time, preventing quantitative determination of the interlayer charge redistribution. These observations motivate a comprehensive DFT study to systematically quantify the charge transfer induced by defects in $4H_b$ -TaS₂ and to determine the identity of the abundantly observed type 2 defects.

In this manuscript, we perform large-scale density functional theory calculations to investigate the impact of defects in $4H_b$ -TaS₂ on its interlayer charge transfer, and to study the nature of experimentally observed type 2 defects. Our study encompasses over 90 defect configurations and includes calculations of defect formation energies, charge transfer, work functions, density of states, and simulated STM images, made publicly available through an online database [33]. By directly comparing STM simulations with experimental observations, we identify three scenarios for the origin of the most abundantly observed type 2 defects: (i) sulfur vacancies located in the buried 1H layer, (ii) tantalum-on-sulfur anti-site defects across the 1T/1H interface, and (iii) Ta interstitials residing between the 1T and 1H layers which exhibit very low formation energies under S-poor conditions. From charge transfer calculations, we find that sulfur vacancies in the 1H layer modify the interlayer charge transfer more strongly than sulfur vacancies in the 1T layer. For Ta_S anti-site defects, we observe particularly strong modulations of charge transfer arising from interlayer bonding between Ta and S atoms across the van der Waals gap, which also stabilizes these defects energetically. From a general perspective, charge transfer between 1T and 1H layers underpins emergent quantum phenomena such as Kondo physics and topological superconductivity, and defects provide a powerful means to locally control this charge transfer. Our extensive simulated dataset thus provides a predictive framework to guide future theoretical and experimental efforts in tailoring the electronic properties of $4H_b$ -TaS₂ via defect engineering.

II. COMPUTATIONAL METHODOLOGY

The following defects have been considered in our study: sulfur vacancies (V_S), tantalum vacancies (V_{Ta}), tantalum interstitials between the layers (Ta_{i1}), Ta_S and

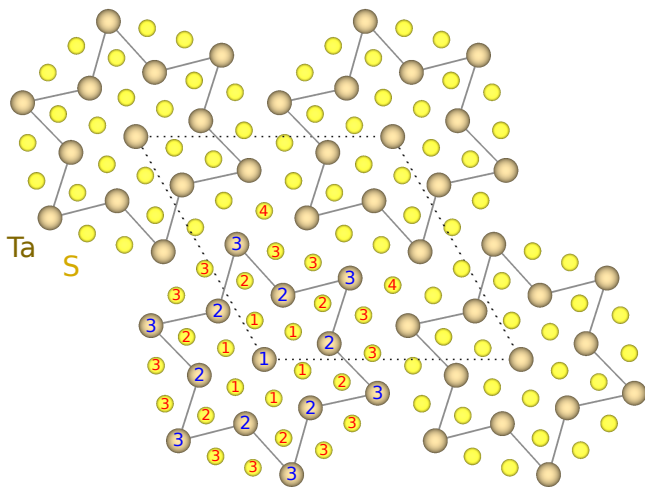


FIG. 3. 1T-TaS₂ monolayer from the top. Brown spheres show tantalum, while the yellow spheres show sulfur. The dotted line marks the charge density wave cell considered. The numbers show different lateral positions of sulfur and tantalum atoms with respect to the tantalum in the center of the star of David (Ta1).

S_{Ta} antisites, as well as oxygen substitutions on sulfur sites (O_S), and iodine substitutions on both sulfur and tantalum sites (I_S and I_{Ta}). Most defects were investigated using a 1T/1H bilayer with a $\sqrt{13} \times \sqrt{13}$ in-plane supercell to accommodate the Star-of-David reconstruction in the 1T layer, consisting of an average of 78 atoms. A 12 Å vacuum is used for all slab calculations in order to eliminate any spurious interactions with the periodic images. Additionally, we examined the four-layer slabs for the pristine case, and a few selected defect cases [see Section A in the Supplemental Material [34]], indicating similar conclusions to the bilayer 1T/1H system. Figure 3 illustrates all possible lateral positions of the tantalum and sulfur atoms relative to the central tantalum atom of the Star-of-David (Ta1), which are used to define various defects. In total, over 90 supercell calculations were carried out.

First-principles calculations are performed based on density functional theory (DFT) using the Vienna *ab initio* Simulation Package (VASP) [35, 36], employing the projector augmented-wave (PAW) approach [37, 38]. The exchange-correlation effects are treated under the generalized gradient approximation (GGA) using the Perdew-Burke-Ernzerhof (PBE) functional [39]. We also calculated the charge density difference using the spherically averaged GGA+*U* [40] ($U_{\text{eff}} = 3$ eV) and GGA+SOC for the pristine 1T/1H bilayer and a few selected defects [see Section B in the Supplemental Material [34]], showing that the difference in calculation details does not alter the qualitative conclusions. The on-site Coulomb interaction of $U_{\text{eff}} = 3$ eV is specifically chosen as the higher limit of the parameter, seeing as previous studies [41–45] have all chosen numbers closer to 2 eV.

The valence configurations for each element are $3s^23p^4$ for S and $5p^65d^46s^1$ for Ta. The non-local van der Waals interaction is modeled by the DFT-D3 method [46]. Structural relaxation is performed until the Hellman-Feynman forces acting on atoms are less than 0.01 eV/Å. The in-plane lattice parameter was obtained by relaxing the pristine bilayer with the Star-of-David distortion and was found to be 12.06 Å. This is in good agreement with the experimental observation of $\sqrt{13} \cdot a \approx 12.01$ Å [47]. Interlayer distances were relaxed in all simulations and were found to vary only slightly; the full values are summarized in Section C1 in the Supplemental Material [34]. The plane-wave energy cut-off is set to 450 eV, and the electronic self-consistency is achieved with a total energy convergence threshold of 10^{-5} eV. A Γ -centered K-point mesh of $12 \times 12 \times 1$ is used for all unitcell calculations, while the $\sqrt{13} \times \sqrt{13}$ SoD CDW structure shown in Fig. 1 is sufficiently converged employing a K-point mesh of $6 \times 6 \times 1$. All calculations were performed with the magnetic moments initialized to zero. This choice was made because initializing finite magnetic moments led to spurious magnetization in the 1H layer for the pristine bilayer and even for bulk 2H-TaS₂, which is experimentally non-magnetic, as well as erratic moment formation in defect supercells that resulted in inconsistent charge transfer values.

To quantify charge transfer (CT) we followed the approach mapped out in Refs. [48–50]. Charge density difference ($e/\text{Å}$) can be defined as:

$$\rho_{\text{diff}}(z) = \rho_{\text{all}}(z) - \sum_{i=1}^N \rho_i(z), \quad (1)$$

where \hat{z} is chosen as the stacking direction, $\rho_{\text{all}}(z)$ is the planar-averaged charge density of the full structure, and $\rho_i(z)$ is the planar-averaged charge density of each constituent; with $i = 1, 2, \dots, N$, where N is the number of the aforementioned components. For each constituent, the charge density is computed while maintaining the atomic positions of the full structure. We then integrate $\rho_{\text{all}}(z)$ in a specified section (z_1, z_2) to determine the total charge difference:

$$q_{\text{diff}}(z_1, z_2) = \int_{z_1}^{z_2} \rho_{\text{diff}}(z) dz. \quad (2)$$

For a given layer, z_1 and z_2 are chosen as the planes midway between the neighboring layers. Here, the z position of each layer is defined by the average z coordinate of the Ta atoms in that layer. In a bilayer, z_1 and z_2 for the 1T layer coincide with z_2 and z_1 for the 1H layer. As a result, the charge gained by 1H is equal in magnitude and opposite in sign to that lost by 1T, so the interlayer charge transfer in the bilayers can be represented by a single value.

For pristine bilayers and for all defect configurations considered above, the bilayer is naturally partitioned into

1T and 1H regions, as the defects can be unambiguously assigned to one of the two layers. An exception arises for Ta interstitial defects, which reside in the interlayer region and cannot be uniquely associated with either layer. In this case, we partition the system into three components: the 1T layer, the 1H layer, and the Ta interstitial. The charge density difference is then defined as $\Delta\rho(z) = \rho_{\text{BL}+\text{Ta}_i}(z) - \rho_{1\text{T}}(z) - \rho_{1\text{H}}(z) - \rho_{\text{Ta}_i}(z)$ where $\rho_{\text{Ta}_i}(z)$ is the plane-averaged charge density of an isolated Ta atom computed at the same atomic position. The charge transfer associated with each layer is subsequently obtained by integrating $\Delta\rho(z)$ over the corresponding spatial region, following the same procedure as described above. We note that this definition captures the asymmetry in charge redistribution between the 1T and 1H layers rather than the total number of electrons donated by the Ta interstitial to each layer. For example, if an isolated Ta atom contributes comparable charge density to both layers, but this balance is slightly modified upon incorporation into the bilayer, the present scheme reflects only the net imbalance between 1T and 1H. This choice is motivated by our focus on interlayer asymmetry, which has been proposed as a key ingredient controlling the emergence of topological superconductivity in this system. If instead one were interested in quantifying the total electron donation of Ta interstitials to each layer individually, an alternative charge partitioning scheme would be required.

We define work function as follows:

$$\text{WF} = eV_{\text{vac}} - E_F, \quad (3)$$

where e is the charge of an electron, V_{vac} the value of the local potential in the vacuum region far from the slab, and E_F the Fermi level of the slab. We then proceed to define the work function differences using the following formula:

$$\Delta\text{WF} = \text{WF}_{1\text{H}} - \text{WF}_{1\text{T}}. \quad (4)$$

A positive ΔWF indicates charge transfer from the 1T layer to 1H, while a negative value promotes this transfer in the opposite direction.

To investigate the likelihood of defect incorporation in the structure, we calculate the formation energy E^f . For a given defect X , the formation energy is defined as:

$$E^f[X] = E_{\text{tot}}[X] - E_{\text{tot}}[\text{TaS}_2] - \sum_i n_i \mu_i, \quad (5)$$

where E_{tot} is the total energy from a supercell calculation, n_i is the number of atoms of atomic species i added to ($n_i > 0$) or removed from ($n_i < 0$) the supercell, and μ_i is the chemical potential that defines the energy added or lost when exchanging atomic species i with its respective reservoir of atoms.

The chemical potential μ_i of each element reflects its relative availability under specific synthesis or processing environments. We define μ_i in reference to the energy of the corresponding elemental phase, such that $\mu_i = \mu_i^0 + \Delta\mu_i$, where μ_i^0 is the total energy of species i in its elemental phase [e.g., solid Ta], and $\Delta\mu_i$ is the deviation from that reference energy. We can then relate values of $\Delta\mu_i$ to the formation enthalpy of TaS_2 through thermodynamic equilibrium:

$$\Delta\mu_{\text{Ta}} + 2\Delta\mu_{\text{S}} = \Delta H_f(\text{TaS}_2) \quad (6)$$

where $\Delta H_f(\text{TaS}_2)$ is calculated to be -5.61 eV. For this we used solid elemental Ta and S_2 gas as a reference. Two extreme limits can now be determined to span the growth or processing circumstances: S-rich (Ta-poor) conditions, where $\Delta\mu_{\text{S}} = 0$; and S-poor (Ta-rich) conditions where $\Delta\mu_{\text{S}} = \frac{1}{2}\Delta H_f(\text{TaS}_2)$. Results will be presented in these limiting conditions, while results for intermediate conditions can be obtained using Eq. 5. For the chemical potentials of oxygen and iodine, we consider the secondary phases Ta_2O_5 and TaI_5 , with the calculated formation enthalpies of -20.01 eV and -3.70 eV, respectively.

STM simulations were visualized using the P4VASP software package based on partial charge density data from VASP. Note that VASP stores the partial charge density in dimensionless units [$\tilde{\rho} = \rho \cdot V$]; therefore, our chosen isosurface value of 0.01 in the software corresponds to a physical charge density of $3.538 \times 10^{-6} \text{ \AA}^{-3}$ for the bilayer supercell ($V = 2826.31 \text{ \AA}^3$). For the 4-layer system ($V = 4694.24 \text{ \AA}^3$), the same software input equates to a physical density of $2.130 \times 10^{-6} \text{ \AA}^{-3}$.

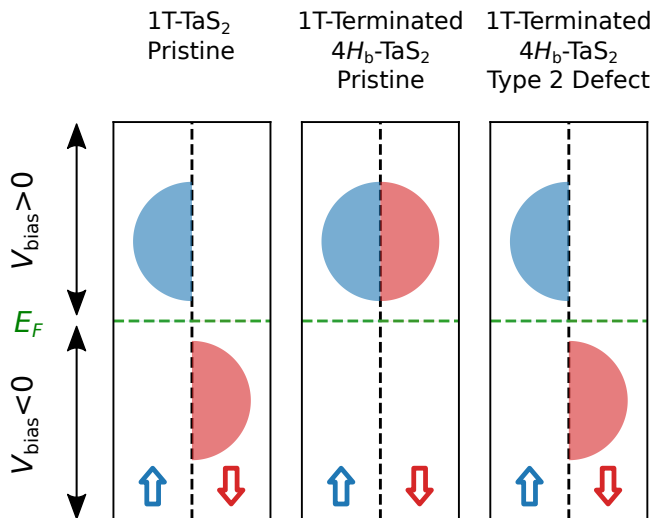
III. RESULTS AND DISCUSSION

A. Sulfur Vacancies

In Ref. [32] we proposed that type 1 defects are S vacancies in the top 1T layer, and type 2 defects are S vacancies in the buried 1H layer. Good comparisons between STM and DFT were presented in Ref. [32] following this scenario, but it leaves open two questions. Why the STM images in Ref. [16, 32] and Fig. 2 show many more type 2 defects than type 1? And what is their influence on the interlayer charge transfer? We first address these two questions within the S vacancy scenario.

1. Defect Identification via STM-DFT Comparison

Given that type 2 defects are the dominant defect in terms of occurrence, it is useful to begin with a simple picture explaining their STM contrast in terms of electron doping, as illustrated in Fig. 4. In 1T-TaS₂, the unpaired electrons at the center of each Star-of-David (SoD) form an effectively half-filled Hubbard model, as



STM intensity contrast 1T-Terminated $4H_b$ -TaS₂

	Pristine	Type 2 Defect
$V_{\text{bias}} > 0$	Reference	Weakly Dim
$V_{\text{bias}} < 0$	Reference	Strongly Bright

FIG. 4. Simple picture explaining 1T-terminated $4H_b$ -TaS₂ STM contrast of type 2 defects and pristine SoD sites at positive and negative biases, in terms of electron doping Hubbard bands. 1T-TaS₂ is a Mott insulator, in pristine $4H_b$ -TaS₂ electrons are doped from 1T to 1H, and in the presence of type 2 defect, an electron is doped in 1T, restoring the Mott insulating state. The green dashed line shows the Fermi level.

shown schematically in the left column of the upper panel of Fig. 4. In pristine $4H_b$ -TaS₂, electrons are transferred from the 1T layer to the 1H layer, resulting in the depopulation of the Hubbard bands in the 1T layer, as shown in the middle column of the upper panel of Fig. 4. In contrast, for SoDs hosting type 2 defects, an additional electron is doped back into the 1T layer, filling one of the Hubbard bands and locally restoring a situation similar to that of pristine 1T-TaS₂, as illustrated in the right column of the upper panel of Fig. 4.

Building on this picture, the STM contrast between pristine SoDs and type 2 defects can be understood using the standard expression for the STM intensity,

$$I(x, y, z) = \int_{E_F}^{E_F + V_{\text{bias}}} \text{LDOS}(E, x, y, z) dE, \quad (7)$$

where x, y, z are the spatial coordinates, E_F is the Fermi energy, V_{bias} is the bias voltage, and LDOS denotes the local density of states. For positive bias, the STM intensity is proportional to the integral of unoccupied states. In pristine SoDs, two empty Hubbard bands

contribute to this integral, whereas for type 2 defects only a single empty Hubbard band is present, explaining why type 2 defects appear dim at positive bias. At negative bias, however, pristine SoDs exhibit no occupied Hubbard bands, while type 2 defects host a Hubbard band below the Fermi level, resulting in an enhancement of the STM intensity.

In addition to the opposite contrast at positive and negative biases, the simple picture in Fig. 2 also explains the experimentally observed asymmetry in magnitude. Type 2 defects appear weakly dim at positive bias but strongly bright at negative bias. This follows naturally from the relative ratios of available states: the ratio of occupied states for type 2 defects to pristine SoDs at negative bias is effectively 1/0, which is much larger than the corresponding ratio of unoccupied states at positive bias of 2/1. In addition to reproducing the STM contrast, this simple picture of a half-filled Hubbard band at type 2 defects is further corroborated by scanning tunneling spectroscopy measurements, which reveal Hubbard bands both below and above the Fermi level, as reported in our previous work [32] and even more clearly in Ref. [16].

Having established a simple picture of type 2 defects as local electron dopers in the 1T layer, we now examine their chemical nature in more detail. Sulfur vacancies are common point defects in transition metal dichalcogenides and act as electron doper, making them a natural candidate within this framework. In Fig. 5, we present first-principles STM simulations for various sulfur-vacancy configurations. To make scanning over many defects manageable, we focus on a single Star-of-David cluster. As a result, comparison between pristine and defect-induced contrast requires separate STM simulations, which are carefully normalized to ensure consistent grayscale height maps. Specifically, identical grayscale values correspond to the same height relative to the surface, defined by the average z position of the top sulfur atoms in the 1T layer. With this procedure, we find that at negative bias the $V_{S1}^{\text{1H(top)}}$ defect reproduces the experimentally observed contrast relative to pristine SoDs: a strong enhancement of brightness appears in contrast to the pristine case. The same qualitative contrast is obtained for sulfur vacancies at the other lateral positions in both the top and bottom sulfur sites of the 1H layer.

So why not assign V_S^{1T} to type 2 defects? These are electron dopers just like V_S^{1H} . However, in addition to contrast, another key characteristic of type 2 defects is that the SoD remains mostly centered and threefold symmetric [see Fig. 2(d) and (f)]. When a sulfur vacancy resides in the exposed 1T layer, it lies close to the local electronic structure directly probed by STM, naturally leading to strong off-centering and/or threefold-symmetry breaking in the STM map, as shown in Fig. 5(e)-(h), regardless of whether V_S^{1T} occupies the top or bottom site of the 1T layer. Such asymmetries are more characteristic of type 1 defects, as shown in Ref. [32] and Fig. 2(e).

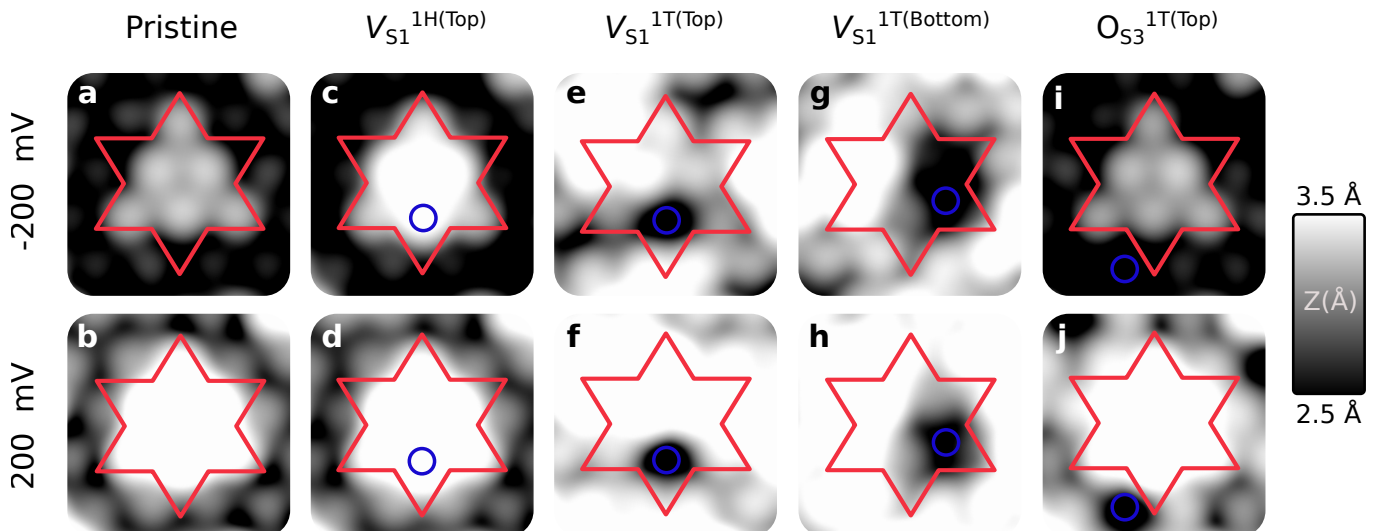


FIG. 5. Scanning tunneling microscopy simulations of the 1T/1H bilayer (a) without defects and with (c) $V_{S1}^{1H(\text{top})}$, (e) $V_{S1}^{1T(\text{top})}$, (g) $V_{S1}^{1T(\text{bottom})}$, and (i) $O_{S3}^{1T(\text{top})}$ at a bias voltage of -200 mV. Panels (b), (d), (f), (h), and (j) show the corresponding simulations for the same configurations at $+200$ mV. The red star and blue circle mark the Star-of-David cluster and the lateral position of the defect, respectively.

This is why in Ref. [32] we assigned type 2 defects to V_S^{1H} and type 1 defects to V_S^{1T} . Another supporting observation is that in Ref. [32] we found that type 1 defects are much easier to manipulate with the STM tip than type 2 defects, consistent with type 1 residing in the exposed 1T layer and type 2 in the buried 1H layer.

TABLE I. Formation energies (E^f) under sulfur-rich and sulfur-poor conditions, charge transfer (CT), and work function difference (ΔWF) for the 1T/1H bilayer in the presence of sulfur vacancies at different positions relative to the tantalum atom at the center of the Star-of-David [see Fig. 3].

Defect	E^f (eV)		CT (e)	ΔWF (eV)
	S-rich	S-poor		
Pristine	N/A	N/A	0.35	0.81
$V_{S1}^{1T(\text{top})}$	3.36	0.56	0.38	0.89
$V_{S2}^{1T(\text{top})}$	3.36	0.56	0.38	0.89
$V_{S3}^{1T(\text{top})}$	3.32	0.52	0.38	0.89
$V_{S4}^{1T(\text{top})}$	3.37	0.57	0.37	0.89
$V_{S1}^{1T(\text{bottom})}$	3.59	0.79	0.34	0.90
$V_{S2}^{1T(\text{bottom})}$	3.48	0.68	0.35	0.91
$V_{S3}^{1T(\text{bottom})}$	3.52	0.72	0.35	0.93
$V_{S4}^{1T(\text{bottom})}$	3.54	0.74	0.35	0.91
$V_{S1}^{1H(\text{top})}$	3.35	0.55	0.23	0.57
$V_{S2}^{1H(\text{top})}$	3.40	0.60	0.24	0.59
$V_{S3}^{1H(\text{top})}$	3.38	0.58	0.24	0.59
$V_{S4}^{1H(\text{top})}$	3.35	0.55	0.24	0.58
$V_{S1}^{1H(\text{bottom})}$	3.28	0.48	0.23	0.58
$V_{S2}^{1H(\text{bottom})}$	3.33	0.53	0.25	0.59
$V_{S3}^{1H(\text{bottom})}$	3.30	0.50	0.25	0.60
$V_{S4}^{1H(\text{bottom})}$	3.29	0.49	0.24	0.60

Despite the consistencies between the experimental observations and the sulfur vacancy scenario, there remain two issues. The first is the question we already raised: why are there many more type 2 defects compared to type 1 defects? In Table I, we present the formation energies of V_S under S-rich and S-poor conditions. The data reveals that vacancies in the 1T(bottom) layer possess formation energies roughly 200 meV higher than those in the 1H or 1T(top) layers, providing a thermodynamical basis for their scarcity. This is consistent with the observation that type 1 defects are easily manipulated by the STM tip, suggesting they are located on the exposed top surface rather than buried. However, 1T(top) energies are comparable to—and sometimes lower than—those of the 1H layer. Furthermore, from a kinetics point of view, sulfur can escape into vacuum from the 1T layer, whereas it remains trapped in 1H beneath the 1T layer. To explain the lack of observed 1T(top) defects, we turn to Ref. [51], which notes that oxygen-chalcogen substitutions can be prolific in TMDs. Even in ultra-high vacuum, the top 1T layer is inevitably exposed to dilute O gas. Since S and O are isovalent, such substitutions are energetically favorable and can “heal” the local electronic structure. Comparing Fig. 5(i)(j) against (a)(b) shows that these (S,O) substitutions strongly mimic pristine SoDs. This could explain why fewer sulfur vacancies are observed in the 1T(top) layer compared to 1H: O substitutions effectively obscure the STM signature of 1T vacancies. We note that for some lateral positions these substitutions shift the peak away from the SoD center while preserving threefold symmetry [see Fig. S12 in the Supplemental Material [34]]. We attribute this to the artifact of simulating periodic rather than dilute, random substitutions. For dilute distributions, we expect

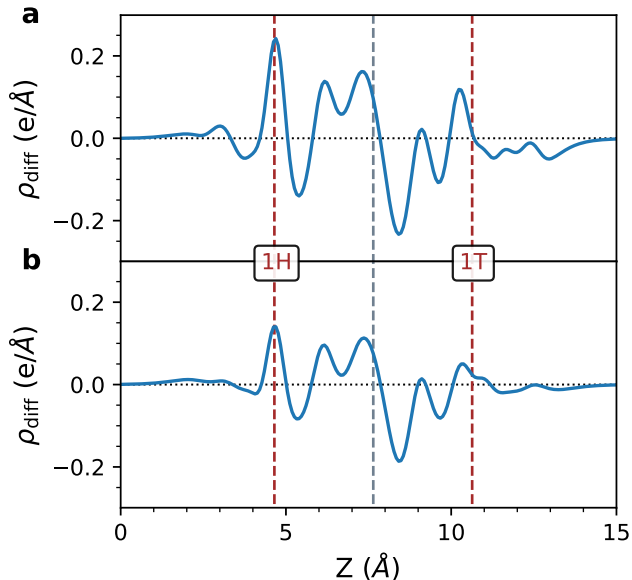


FIG. 6. Charge density difference for (a) pristine 1T/1H bilayer and (b) 1T/1H bilayer with $V_{S1}^{1H(\text{top})}$, a sulfur vacancy in the top of the 1H layer. Brown dashed lines show the average height of Ta atoms for each layer, while the grey dashed line is the midpoint between the two layers.

the surrounding pristine SoDs to restore the peak in the defected SoD to its original center.

The second issue with interpreting type 2 defects as sulfur vacancies in 1H is that, while the strong brightness contrast at negative bias is reproduced, the corresponding dimness at positive bias is not captured in the simulations shown in Fig. 5(a)-(d). We note that this contrast is intrinsically more difficult to reproduce, since it is a weaker effect than the pronounced brightness at negative bias, consistent with the discussion above in terms of the relative ratios of available states at positive and negative bias.

2. Interlayer Charge Transfer Modulation

One of the exciting possibilities of defect manipulation reported in Ref. [32] is that it opens the door to local tuning of charge transfer, which in turn can be used to modify the exotic properties of $4H_b$ -TaS₂. While such charge transfer effects are qualitatively suggested by STM in Ref. [32], quantitatively extracting these via this technique is difficult. Although changes in local charge influence the STM height, the measured signal also incorporates effects from electronic wave functions and atomic structure, complicating quantitative interpretation. Therefore, to directly quantify how S vacancies modify the interlayer charge transfer, we perform DFT calculations.

To quantify the charge transfer modulation, we com-

pute the difference between the charge of the full bilayer and the charges of the individual layers, following the procedure of Ref.[48–50]. We first planar-average this difference and then integrate it within the 1T and 1H regions. These regions are defined by planes midway between the 1T and 1H layers, which in turn are determined from the average Ta z positions [see Section II for more details]. In Fig. 6 we show the results for the pristine bilayer and for a sulfur vacancy in the top of the 1H layer, $V_{S1}^{1H(\text{top})}$. In Fig. 6(a), the planar-averaged density difference in units of electron charge is mostly positive in the 1H region and mostly negative in the 1T region, representing the charge transfer from 1T to 1H. In Fig. 6(b), these positive and negative fluctuations are reduced, demonstrating that the sulfur vacancy in 1H suppresses the charge transfer from 1T to 1H. This is expected, since sulfur vacancies in 1H effectively donate extra electrons that block the charge transfer from 1T. This finding is also consistent with the simple picture described in Fig. 4, in which sulfur vacancies in 1H act like type 2 defects that inhibit charge transfer and restore the central 1T Ta- dz^2 electrons to their half-filled Hubbard band state.

If we integrate the planar-averaged charge density modulations in Fig. 6 over the 1H region, we obtain values $0.35 e$ and $0.23 e$ for the pristine bilayer, and the bilayer with a sulfur vacancy in 1H, respectively. By definition, the opposite values are obtained when integrating over the 1T region. This shows that the sulfur vacancy in 1H reduces the interlayer charge transfer by $0.12 e$. In Table I, we list the numerical values for the charge transfers for all S vacancies. Corresponding planar-averaged density difference plots are shown in Fig. S18 in the Supplementary Material [34]. Two points are noteworthy. First, the lateral position of the vacancy does not significantly influence the charge transfer. On the other hand, there is a substantial difference in charge transfer modulation depending on whether the vacancy resides in 1T or 1H. The sign of the modulation is opposite, as expected: placing a vacancy in 1T effectively injects an extra electron into 1T, which enhances the charge transfer. The less expected observation is that the magnitude of the charge transfer modulation induced by a sulfur vacancy in 1T is roughly an order of magnitude smaller than that by a sulfur vacancy in 1H.

We are not entirely certain why there is a pronounced asymmetry in the magnitude of the charge transfer modulation between vacancies in 1T and 1H. However, we have identified two clues. First, the charge transfer correlates with the difference in work function between the two layers. For the pristine bilayer, the work functions computed for the individual 1T and 1H layers are 5.11 eV and 5.93 eV, respectively, giving a difference of 0.81 eV. This misalignment of Fermi levels is consistent with the direction of charge transfer from 1T to 1H. As shown in Table I, sulfur vacancies in 1H reduce the work-function difference between 1T and 1H by about 0.22–0.24 eV, whereas sulfur vacancies in 1T increase the work function by only ~ 0.08 – 0.12 eV. This is mirroring the trend ob-

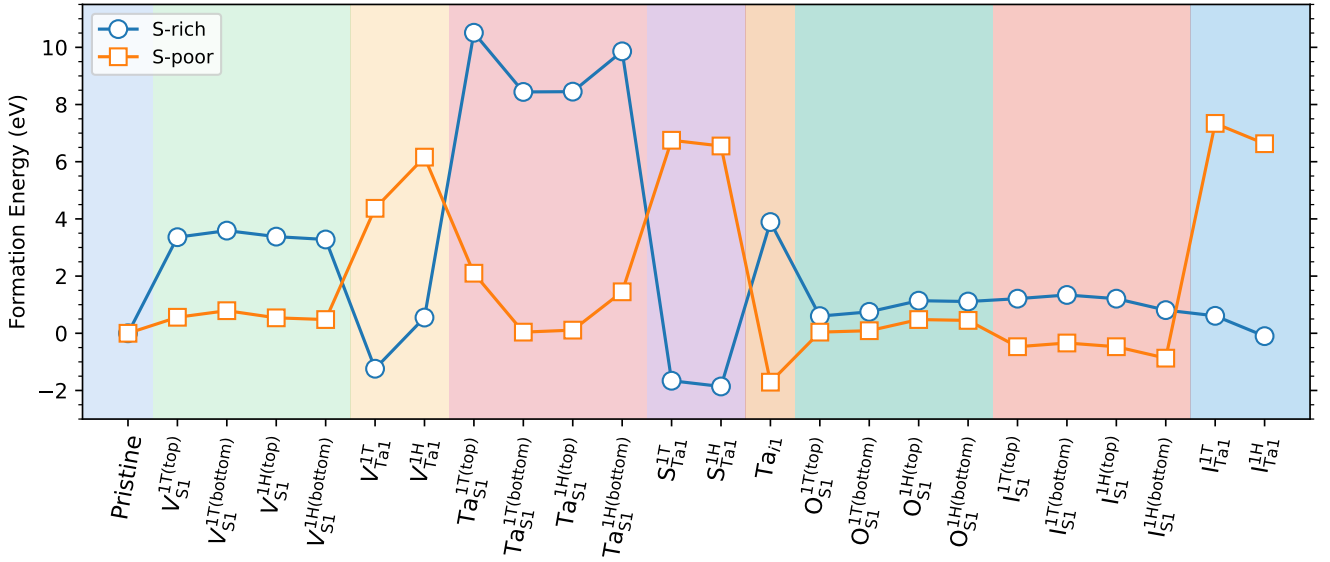


FIG. 7. Formation energies in S-poor and S-rich conditions for pristine 1T/1H bilayers and bilayers with various single defects. We show one representative lateral position per vertical site, as vertical position dominates the formation energy.

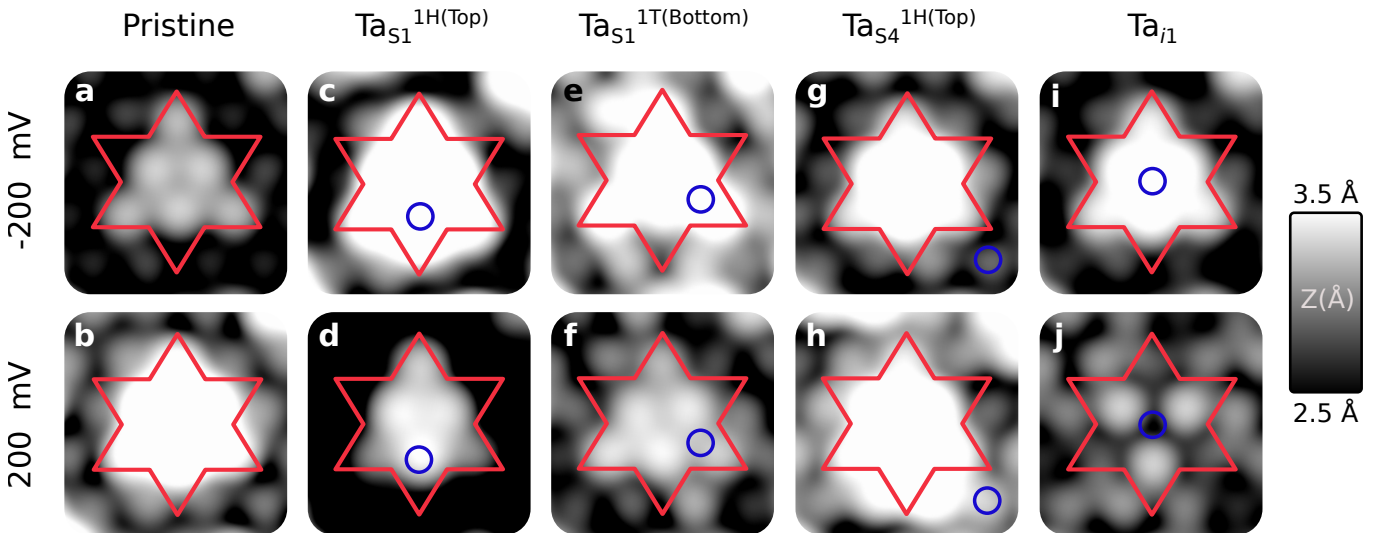


FIG. 8. Scanning tunneling microscopy simulations of the 1T/1H bilayer (a) without defects and with Ta on S anti-site defects (c) $\text{Ta}_{\text{S1}}^{1\text{H}(\text{top})}$, (e) $\text{Ta}_{\text{S1}}^{1\text{T}(\text{bottom})}$, (g) $\text{Ta}_{\text{S4}}^{1\text{H}(\text{top})}$, and Ta interstitial (i) Ta_{i1} at a bias voltage of -200 mV. Panels (b), (d), (f), (h), and (j) show the corresponding simulations for the same configurations at $+200$ mV. The red star and blue circle mark the Star-of-David cluster and the lateral position of the defect, respectively.

served for the charge transfer in terms of both sign and magnitude. Second, if the $V_{\text{S1}}^{1\text{H}}$ induced atomic relaxations are excluded from our 1T/1H bilayer simulation, the charge transfer becomes $0.31 e$, significantly closer to the pristine value than in the fully relaxed case ($0.23 e$). This shows that structural relaxation plays an important role in the larger change in charge transfer caused by 1H vacancies compared to 1T vacancies.

B. Other Defects

In Ref. [32] and in the discussion in this manuscript so far, we have proposed that type 2 defects can be explained in terms of sulfur vacancies. However, many other native defects are possible. We therefore also consider Ta vacancies, antisite defects (Ta_{S} and S_{Ta}) at all lateral positions, as well as Ta interstitials located at various lateral positions between the 1T and 1H layers. In addition, we examine iodine substitutions on S and Ta sites,

motivated by the use of iodine as a transport agent in the chemical vapor transport growth of $4H_b$ -TaS₂. Fig. 7 provides an overview of the formation energies of these defects, where a representative lateral position is shown for each defect type, as lateral variations are comparatively small. The full results are presented in Tables I and II and Section C3 of the Supplementary Material [34]. We emphasize that while formation energies offer useful guidance, they do not provide a complete picture of defect populations in chemically vapor-transport-grown $4H_b$ -TaS₂, as the growth process is inherently non-equilibrium and influenced by chemical reactions, gas-phase chemical potentials, transport gradients, and kinetic barriers. To further identify which of these defects are realized experimentally, we therefore turn again to a comparison between DFT simulations and STM measurements.

1. Defect Identification via STM-DFT Comparison

Among the other native defects besides sulfur vacancies, Ta-on-S antisites are an interesting possibility because, like sulfur vacancies, they act as electron dopants. Interestingly, we see from Fig. 8(a)-(d) that some Ta-on-S antisites in the top of the 1H layer, such as Ta_{S1}^{1H(top)}, produce the correct contrast at both positive and negative bias. However, some other Ta-on-S antisite defects, such as those located in the bottom of 1T [e.g., Ta_{S2}^{1T(bottom)}], do not reproduce the STM image correctly. These defects appear bright compared to pristine at positive bias and, notably, are strongly off-centered relative to the SoD center and/or lack threefold symmetry [see Fig. S8 in the Supplemental Material [34]]. Not all defects in 1T produce a poor match, though. For example, Ta_{S1}^{1T(bottom)}, shown in Fig. 8(e)(f), exhibits the correct contrast and a peak located at the center of the SoD. Conversely, some Ta-on-S antisites in 1H top, such as Ta_{S4}^{1H(top)}, display the wrong contrast compared to experiment. Although centered closely to the SoD, it appears bright rather than dim relative to pristine SoD at positive bias, as shown in Fig. 8(b)-(h).

To better understand how the experimentally observed STM contrast compares with the Ta_S antisite simulations, we next turn to their defect formation energies listed in Table II, which include the full set of lateral configurations for each vertical site. While formation energies alone cannot determine defect populations in chemically vapor-transport-grown $4H_b$ -TaS₂, owing to non-equilibrium growth conditions and kinetic effects, they provide a more stringent criterion when comparing defects of the same type. We therefore proceed to use the formation energies to assess the relative likelihood of different Ta_S configurations. We observe a clear trend: Ta_S antisites located between the layers [bottom 1T or top 1H] have significantly lower formation energies than Ta_S antisites at the exposed surfaces of the bilayer [top 1T and bottom 1H]. We find that this energetic preference

TABLE II. Formation energies (E^f) under sulfur-rich and sulfur-poor conditions, charge transfer (CT), and work function difference (ΔWF) for the 1T/1H bilayer in the presence of Ta on S anti-site defects and Ta interstitials at different positions relative to the tantalum atom at the center of the star of David [see Fig. 3]. The lowest formation energies are highlighted in bold; these defects reproduce the characteristic STM contrasts compared to pristine stars of David, as observed in STM experiments [compare Fig. 8(a)-(f) and (i)(j) against Fig. 2(d)(f)].

Defect	E^f (eV)		CT (e)	ΔWF (eV)
	S-rich	S-poor		
Ta _{S1} ^{1T(top)}	10.51	2.10	0.27	0.67
Ta _{S2} ^{1T(top)}	10.48	2.07	0.29	0.74
Ta _{S3} ^{1T(top)}	10.53	2.12	0.28	0.71
Ta _{S4} ^{1T(top)}	10.48	2.07	0.29	0.70
Ta_{S1}^{1T(bottom)}	8.45	0.04	0.65	0.86
Ta _{S2} ^{1T(bottom)}	8.57	0.16	0.60	0.85
Ta _{S3} ^{1T(bottom)}	8.58	0.17	0.60	0.85
Ta _{S4} ^{1T(bottom)}	8.57	0.16	0.60	0.85
Ta_{S1}^{1H(top)}	8.44	0.03	-0.15	0.43
Ta _{S2} ^{1H(top)}	8.71	0.30	-0.18	0.23
Ta _{S3} ^{1H(top)}	8.50	0.09	-0.13	0.44
Ta _{S4} ^{1H(top)}	8.95	0.54	-0.03	0.17
Ta _{S1} ^{1H(bottom)}	9.86	1.45	0.24	0.65
Ta _{S2} ^{1H(bottom)}	9.87	1.46	0.25	0.66
Ta _{S3} ^{1H(bottom)}	9.87	1.46	0.25	0.66
Ta _{S4} ^{1H(bottom)}	9.86	1.45	0.25	0.66
Ta_{i1}	3.89	-1.72	0.33	0.72
Ta _{i2}	4.08	-1.53	0.31	0.70
Ta _{i3}	4.01	-1.60	0.26	0.63

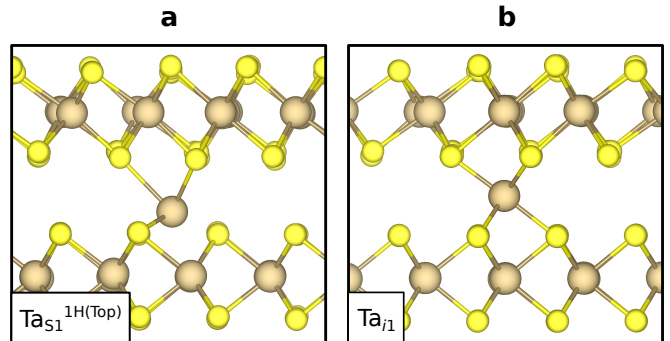


FIG. 9. Structures of 1T/1H bilayer with (a) Ta on S anti-site Ta_{S1}^{1H(top)} displaying bonding with the bottom 1T S atoms, and (b) the Ta interstitial Ta_{i1}. Brown spheres show tantalum, while the yellow spheres show sulfur.

arises because a Ta_S at the bottom of the 1T layer can move a bit out of the layer and bond with sulfur atoms in the top of the 1H layer, and vice versa. This bonding configuration is illustrated in the side-view structural schematic shown in Fig. 9(a).

We thus find that Ta_S antisites located between the 1T and 1H layers have significantly lower formation en-

ergies, due to the energy gained from Ta bonding with sulfur atoms in the opposing 1T or 1H layer. Nonetheless, this alone does not explain the observed STM intensities, because not all Ta_S defects between the layers reproduce the correct STM contrast. For example, in Fig. 8(b)(h) we see that $\text{Ta}_{S_4}^{1\text{H}(\text{top})}$ displays the wrong contrast at positive bias. However, among the Ta_S defects located between the layers, those with the lowest formation energies are precisely the ones that yield the correct STM contrast: in the S-poor limit, $\text{Ta}_{S_1}^{1\text{H}(\text{top})}$ and $\text{Ta}_{S_1}^{1\text{T}(\text{bottom})}$ have formation energies of 0.03 eV and 0.04 eV, respectively. These defects are highlighted in bold in Table II. The next higher-energy defect, $\text{Ta}_{S_3}^{1\text{H}(\text{top})}$ with a formation energy of 0.09 eV in the S-poor limit, also reproduces the correct STM contrast, albeit with a slightly off-centered peak relative to the Star-of-David [see Fig. S9 in the Supplementary Material [34]]. In contrast, $\text{Ta}_{S_4}^{1\text{H}(\text{top})}$ has a formation energy of 0.16 eV in the S-poor limit and exhibits the incorrect contrast at positive bias [see also Fig. S9 in the Supplementary Material [34]]. Thus, in the S-poor limit, Ta_S defects that produce the wrong STM contrast have formation energies roughly four times higher than those that reproduce the experimentally observed contrast, which may explain why such defects are not observed experimentally.

In addition to Ta-on-S antisites, Ta interstitials are also electron dopers and are therefore interesting candidates for the type 2 defects. By comparing Fig. 8(a,b) and Fig. 8(i,j), we find that the Ta_{i1} interstitial [located above Ta_1 , as defined in Fig. 3] exhibits the correct STM contrast, appearing bright (dim) at negative (positive) bias, with a peak centered on the SoD. In contrast, Ta interstitials at other lateral positions [Ta_{i2} and Ta_{i3}] show the wrong contrast and display peaks that are off-centered relative to the SoD and/or not threefold symmetric. As in the case of Ta_S defects, we find that the Ta interstitial exhibiting the correct STM contrast also has the lowest formation energy [highlighted in bold in Table II], whereas the higher-energy Ta interstitials correspond to the incorrect STM signatures. This energetic ordering may therefore explain why Ta_{i2} and Ta_{i3} are not observed experimentally, particularly under growth conditions intermediate between S-rich and S-poor, where the formation energy of Ta_{i1} is close to zero. We note that Ta interstitials below S sites were also considered but were found to be unstable or to have prohibitively high formation energies.

We also performed STM simulations for other native defects, including S_{Ta} antisites and Ta vacancies. However, none of these defects show good agreement with the experimental STM images, either in terms of the bias-dependent contrast or the position of the intensity maximum [see Section C2 in the Supplementary Material [34]]. In addition, we considered iodine substitutions on sulfur sites, motivated by the use of iodine as a transport agent in the chemical vapor transport growth of the crystal. Since I for S substitutions act as electron dopers, they

could in principle be suitable candidates for type 2 defects. However, their simulated STM signatures do not reproduce the experimental observations [see Fig. S14 in the Supplementary Material [34]]. This leaves Ta_S antisites and Ta interstitials as the most plausible candidates for type 2 defects, in addition to the previously discussed sulfur vacancies.

2. Interlayer Charge Transfer Modulation

To provide an overview of how different defects can be used to engineer the interlayer charge transfer in $4H_b$ - TaS_2 , we summarize in Fig. 10 the charge transfer induced by all defects relative to the pristine bilayer, together with the corresponding work-function differences. Corresponding planar-averaged density difference plots are shown in Section C4 in the Supplementary Material [34]. The most striking feature is that Ta_S antisites located between the layers induce exceptionally large modulations of the interlayer charge transfer, with a strong dependence on whether the defect resides in the 1T or 1H layer. A Ta_S antisite in 1T roughly doubles the charge transfer, increasing it from about 0.35 to 0.7 electrons per Star-of-David cluster, whereas a Ta_S antisite in 1H reverses the direction of charge transfer, with approximately 0.1 electrons flowing from 1H to 1T. The origin of these pronounced charge-transfer modulations can again be traced to the bonding between the Ta_S antisite and sulfur atoms in the opposite layer, as illustrated in Fig. 9(a). Through these bonds, a Ta_S antisite in 1H injects electrons into the 1T layer, and vice versa for a Ta_S antisite in 1T. Consequently, the strong charge-transfer effects and the low formation energies of these defects share a common physical origin.

Another remarkable feature of Fig. 10 is the strong correlation between the charge transfer and the work-function difference. This indicates that, at least to some extent, the interlayer charge transfer is governed by electrostatic alignment arising from the work-function mismatch between the individual 1T and 1H layers, rather than being dominated purely by interlayer hybridization or interactions. Defects locally modify the intrinsic electronic properties of each layer, and the resulting charge transfer reflects these layer-resolved changes. Interlayer coupling still plays an important role, particularly for Ta_S antisites and Ta interstitials where strong bonding occurs between opposite layers, but the correlation between the charge transfer and the work-function difference in Fig. 10 shows that individual layer energetics constitute a key driving force.

C. Hybridization Effects on Charge Transfer

Lastly, we wish to comment on an important aspect of the charge transfer analysis related to hybridization between states in the 1T and 1H layers. In Fig. 11(a), the

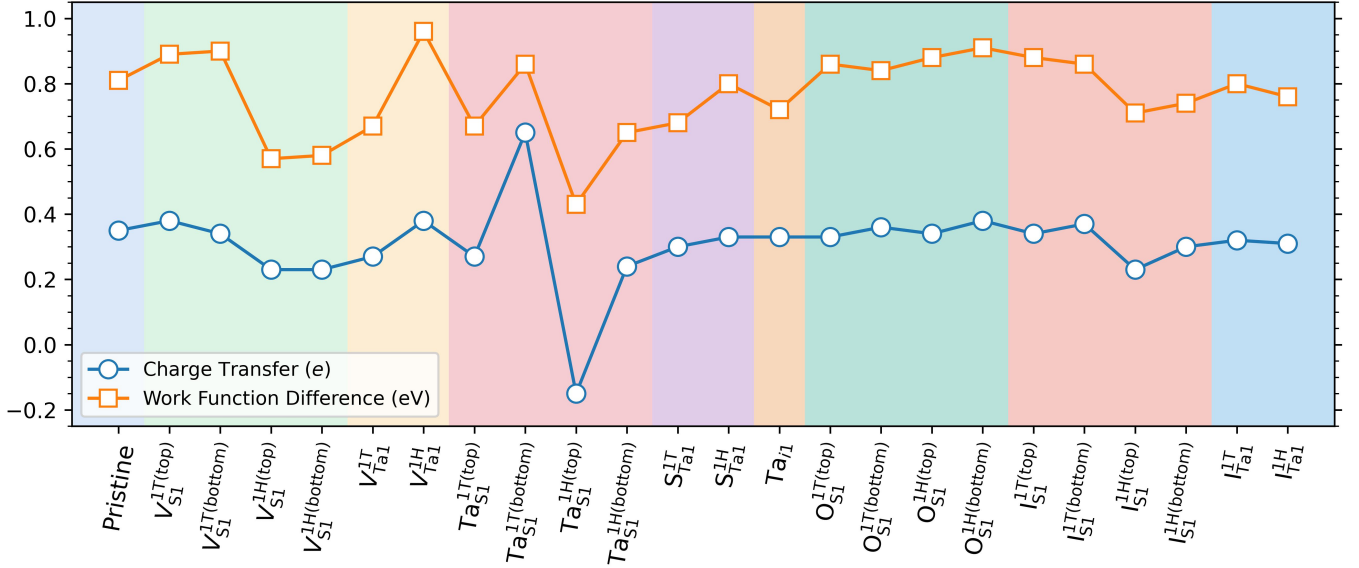


FIG. 10. Comparison of work function difference and charge transfer for pristine 1T/1H bilayers and bilayers with various single defects. Only one defect per vertical position is shown, as lateral displacement has little effect. Outliers significantly higher than the lateral average are $O_{S3}^{1T(top)}$ and $O_{S4}^{1T(top)}$ (see Tables I and II and Tables S5-S7 in the Supplemental Material [34]).

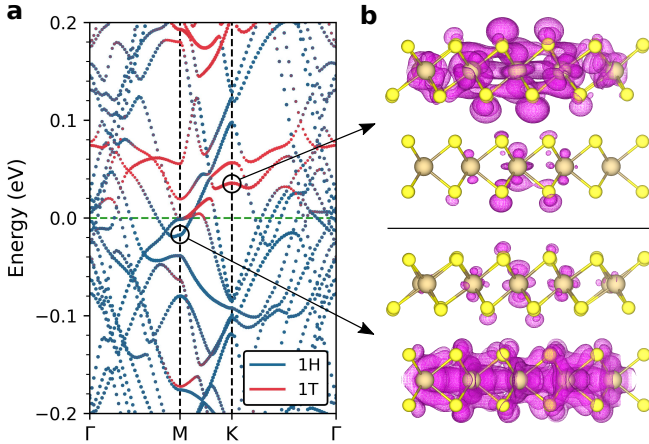


FIG. 11. (a) Band structure of pristine 1T/1H bilayer. Contributions from each layer are given, with the 1T layer shown in red and the 1H layer shown in blue. The green dashed line shows the Fermi level. (b) Charge densities of the selected points in the band structure. Brown spheres show tantalum, while the yellow spheres show sulfur. Iso-surface values are set to 0.0002 1/\AA^3 .

band structure of the pristine 1T/1H bilayer is shown, with contributions from each layer indicated by different colors. In Fig. 11(b), we plot the real-space charge densities of selected Bloch states, where a noticeable degree of hybridization between the two layers can be observed. By integrating the charge density of the wave functions within the 1T and 1H layers, we find that approximately 10% of the charge density of Bloch states predominantly

associated with one layer resides in the opposite layer.

This hybridization is non-negligible. For example, if a sulfur vacancy were to donate two electrons into bands predominantly associated with the 1T layer, about 0.2 of these electrons would reside in the 1H layer. This value is comparable to the charge transfer magnitudes reported in this work for several defects. In the charge transfer analysis, this portion of electrons would therefore be counted as occupying the 1H layer, even though in this thought experiment the electrons were introduced entirely into the 1T-derived bands. This illustrates an intrinsic aspect of charge partitioning in hybridized systems that should be kept in mind, particularly when making comparisons with angle-resolved photoemission spectroscopy, STM experiments, or model-based approaches such as doped Hubbard calculations.

IV. CONCLUSION AND OUTLOOK

$4H_b$ -TaS₂ is an intriguing system because it couples superconductivity in the 1H layer with the Star-of-David charge-density wave in the 1T layer. Interlayer charge transfer has been proposed as a key ingredient for topological superconductivity, and STM experiments have shown that defects can be created or removed, thereby opening the door to local tuning the charge transfer and the exotic properties of $4H_b$ -TaS₂. The dominant defects in this material have been classified as type 2 defects, but their precise identification has remained challenging. In this work, we adopt a holistic approach, simulating over 90 defect configurations to identify the most plausi-

ble scenarios. Based on this analysis, we identified three candidates for type 2 defects: (i) sulfur vacancies in the 1H layer, where oxygen substitutions may explain the absence of V_S^{1T} in STM, although simulations do not capture the observed dimness at positive bias; (ii) Ta-on-S antisites; and (iii) Ta interstitials. Notably, for both Ta-based defects, the energetically preferred lateral positions are precisely those that reproduce the experimental STM contrast across both bias polarities.

Several experimental strategies could help distinguish these scenarios. The oxygen concentration in the cleaving station or STM chamber could be varied to test its effect on the type 1/type 2 defect ratio. Higher-resolution STM could resolve atomistic details within the Star-of-David clusters to distinguish pristine S sites from O_S substitutions as has been done in Ref. [51]. Cross-sectional scanning transmission electron microscopy (STEM) could identify Ta atoms above S sites for Ta-on-S antisites or within the van der Waals gap for Ta interstitials [see Fig. 9]. Notably, because these defects occur at a 10% frequency relative to the 13 Ta atoms in a cluster, the resulting signal from these specific Ta columns would be significantly weaker than a standard Ta column, requiring high-sensitivity imaging to detect.

Regardless of the specific nature of the type 2 defects, our calculations show that formation energies vary strongly with growth conditions [S-poor versus S-rich], suggesting an opportunity for engineering of charge transfer by tuning the chemical potential. In particular, Ta-on-S antisites strongly influence the interlayer charge transfer, providing a pathway to modulate the exotic electronic properties of $4H_b$ -TaS₂. To support further work, all input and output files from this study have been made publicly available in an online database [33]. This systematic first-principles dataset facilitates the understanding of defect-induced charge transfer in $4H_b$ -TaS₂ and serves as a comprehensive reference for future theoretical, experimental, and data-driven investigations.

AUTHOR CONTRIBUTIONS

S.K., T.B., and S.M. conceptualized the project and wrote the manuscript. S.K. performed the calculations under the supervision of T.B. and S.M.. W.Y., W.K. and A.P.L. conducted the STM experiments. H.D.Z. carried out the crystal growth.

ACKNOWLEDGMENTS

This work was conducted at the Center for Nanophase Materials Sciences (CNMS), which is a U.S. Department of Energy, Office of Science User Facility. S.M. would like to acknowledge the startup fund from the University of South Carolina. This research used resources of the National Energy Research Scientific Computing Center (NERSC), a Department of Energy User Facility using NERSC award BES-ERCAP0035988. We also used the Expanse supercomputer at the San Diego Supercomputer Center through allocation PHY230093 from the Advanced Cyberinfrastructure Coordination Ecosystem: Services & Support (ACCESS) program, which is supported by National Science Foundation Grants No. 2138259, No. 2138286, No. 2138307, No. 2137603, and No. 2138296. The crystal growth (H.D.Z) was supported by the U.S. Department of Energy (DOE) under Grant No. DE-SC0020254.

This manuscript has been authored by UT-Battelle, LLC under Contract No. DE-AC05-00OR22725 with the U.S. Department of Energy. The United States Government retains and the publisher, by accepting the article for publication, acknowledges that the United States Government retains a non-exclusive, paid-up, irrevocable, world-wide license to publish or reproduce the published form of this manuscript, or allow others to do so, for United States Government purposes. The Department of Energy will provide public access to these results of federally sponsored research in accordance with the DOE Public Access Plan (<http://energy.gov/downloads/doe-public-access-plan>).

CONFLICT OF INTEREST

The authors declare no conflict of interest.

-
- [1] K. T. Law and P. A. Lee, *Proc. Natl. Acad. Sci.* **114**, 6996 (2017).
 - [2] B. Sipos, A. F. Kusmartseva, A. Akrap, H. Berger, L. Forró, and E. Tutiš, *Nat. Mater.* **7**, 960 (2008).
 - [3] L. Cheng, X. Long, X. Chen, X. Zou, and Z. Liu, *Phys. Rev. B* **104**, L241114 (2021).
 - [4] P. Fazekas and E. Tosatti, *Physica B+C* **99**, 183 (1980).
 - [5] K. Rossnagel and N. V. Smith, *Phys. Rev. B* **73**, 073106 (2006).
 - [6] W. Ruan, Y. Chen, S. Tang, J. Hwang, H.-Z. Tsai, R. L. Lee, M. Wu, H. Ryu, S. Kahn, F. Liou, C. Jia, A. Aikawa, C. Hwang, F. Wang, Y. Choi, S. G. Louie, P. A. Lee, Z.-X. Shen, S.-K. Mo, and M. F. Crommie, *Nat. Phys.* **17**, 1154 (2021).

- [7] H. Dong, P. Sun, L. Lei, Y. Geng, J. Guo, Y. Li, L. Huang, R. Xu, F. Pang, W. Ji, W. Zhou, Z. Liu, Z.-Y. Lu, H.-J. Gao, K. Liu, and Z. Cheng, (2023), [arXiv:2301.05885](https://arxiv.org/abs/2301.05885) [cond-mat.mtrl-sci].
- [8] Y. Geng, H. Dong, R. Wang, J. Guo, S. Mi, L. Lei, Y. Li, L. Huang, F. Pang, R. Xu, W. Yu, H.-J. Gao, W. Ji, W. Zhou, and Z. Cheng, *ACS Nano* **19**, 7784 (2025).
- [9] Y. Geng, L. Lei, H. Dong, J. Guo, S. Mi, Y. Li, L. Huang, F. Pang, R. Xu, W. Zhou, Z. Liu, W. Ji, and Z. Cheng, *Phys. Rev. B* **107**, 195401 (2023).
- [10] S. C. de la Barrera, M. R. Sinko, D. P. Gopalan, N. Sivadas, K. L. Seyler, K. Watanabe, T. Taniguchi, A. W. Tsun, X. Xu, D. Xiao, and B. M. Hunt, *Nat. Commun.* **9**, 1427 (2018).
- [11] Y. Yang, S. Fang, V. Fatemi, J. Ruhman, E. Navarro-Moratalla, K. Watanabe, T. Taniguchi, E. Kaxiras, and P. Jarillo-Herrero, *Phys. Rev. B* **98**, 035203 (2018).
- [12] V. Vaño, S. C. Ganguli, M. Amini, L. Yan, M. Khosravian, G. Chen, S. Kezilebieke, J. L. Lado, and P. Liljeroth, *Adv. Mater.* **35**, 2305409 (2023).
- [13] C.-S. Lian, C. Heil, X. Liu, C. Si, F. Giustino, and W. Duan, *Phys. Rev. B* **105**, L180505 (2022).
- [14] D. Zhang, Y. Wu, Y.-H. Su, M.-C. Hsu, C. Ó Coileáin, J. Cho, M. Choi, B. S. Chun, Y. Guo, C.-R. Chang, and H.-C. Wu, *IUCrJ* **7**, 913 (2020).
- [15] R. V. Coleman, G. K. Eiserman, S. J. Hillenius, A. T. Mitchell, and J. L. Vicent, *Phys. Rev. B* **27**, 125 (1983).
- [16] A. K. Nayak, A. Steinbok, Y. Roet, J. Koo, I. Feldman, A. Almoalem, A. Kanigel, B. Yan, A. Rosch, N. Avraham, and H. Beidenkopf, *Proc. Natl. Acad. Sci.* **120**, e2304274120 (2023).
- [17] S. Shen, T. Qin, J. Gao, C. Wen, J. Wang, W. Wang, J. Li, X. Luo, W. Lu, Y. Sun, and S. Yan, *Chin. Phys. Lett.* **39**, 077401 (2022).
- [18] S.-Z. Lin, *Phys. Rev. Res.* **6**, 023224 (2024).
- [19] C. Wen, J. Gao, Y. Xie, Q. Zhang, P. Kong, J. Wang, Y. Jiang, X. Luo, J. Li, W. Lu, Y.-P. Sun, and S. Yan, *Phys. Rev. Lett.* **126**, 256402 (2021).
- [20] P. Wu, Z. Wang, Y. Zhang, Z. Chen, S. Yu, W. Ma, M. Shan, Z. Liang, X. Wei, J. Wang, W. Cheng, Z. Liang, X. Zhang, T. Wu, Y. Okada, K. Jiang, Z. Wang, and X. Chen, (2025), [arXiv:2508.17861](https://arxiv.org/abs/2508.17861) [cond-mat.supr-con].
- [21] M. Date, H. Bae, A. Louat, G. Domaine, N. B. M. Schröter, E. D. Como, B. Yan, and M. D. Watson, *Commun. Phys.* **9**, 60 (2026).
- [22] Z. Haoyan, G. Jianfeng, M. Shuo, L. Songyang, and C. Zhihai, *Chin. J. Vac. Sci. Technol.* **43**, 825 (2023).
- [23] J. J. Gao, J. G. Si, X. Luo, J. Yan, Z. Z. Jiang, W. Wang, Y. Y. Han, P. Tong, W. H. Song, X. B. Zhu, Q. J. Li, W. J. Lu, and Y. P. Sun, *Phys. Rev. B* **102**, 075138 (2020).
- [24] J. Bang, B. Lee, H. Yang, S. Kim, D. Wulferding, and D. Cho, *Phys. Rev. B* **109**, 195170 (2024).
- [25] C. G. Ayani, M. Bosnar, F. Calleja, A. P. Solé, O. Stetsovych, I. M. Ibarburu, C. Rebanal, M. Garnica, R. Miranda, M. M. Otrokov, M. Ondráček, P. Jelínek, A. Arnau, and A. L. Vázquez de Parga, *Nano Lett.* **24**, 10805 (2024).
- [26] L. Crippa, H. Bae, P. Wunderlich, I. I. Mazin, B. Yan, G. Sangiovanni, T. Wehling, and R. Valentí, *Nat. Commun.* **15**, 1357 (2024).
- [27] H. Bae, R. Valentí, I. I. Mazin, and B. Yan, *npj Quantum Mater.* **10**, 92 (2025).
- [28] Y. Geng, M. Wang, S. Meng, S. Mi, C. Li, H. Hu, J. Guo, R. Xu, F. Pang, W. Ji, W. Zhou, and Z. Cheng, *Chin. Phys. Lett.* **43**, 030705 (2026).
- [29] A. Ribak, R. M. Skiff, M. Mograbi, P. K. Rout, M. H. Fischer, J. Ruhman, K. Chashka, Y. Dagan, and A. Kanigel, *Sci. Adv.* **6**, eaax9480 (2020).
- [30] I. Silber, S. Mathimalar, I. Mangel, A. K. Nayak, O. Green, N. Avraham, H. Beidenkopf, I. Feldman, A. Kanigel, A. Klein, M. Goldstein, A. Banerjee, E. Sela, and Y. Dagan, *Nat. Commun.* **15**, 824 (2024).
- [31] A. K. Nayak, A. Steinbok, Y. Roet, J. Koo, G. Margalit, I. Feldman, A. Almoalem, A. Kanigel, G. A. Fiete, B. Yan, Y. Oreg, N. Avraham, and H. Beidenkopf, *Nat. Phys.* **17**, 1413 (2021).
- [32] W. Yang, S. Karbasizadeh, H. Jeon, S. Hus, A. P. Badorf, S. Mu, T. Berlijn, H. Zhou, W. Ko, and A.-P. Li, *Phys. Rev. B* **112**, 245126 (2025).
- [33] Author(s), Computational Data for Defect Engineering in 4Hb-TaS₂, *Zenodo Repository* (2025), online data repository.
- [34] Supplementary Information: <https://www.your-link-here.com>.
- [35] G. Kresse and J. Hafner, *Phys. Rev. B* **48**, 13115 (1993).
- [36] G. Kresse and J. Furthmüller, *Phys. Rev. B* **54**, 11169 (1996).
- [37] P. E. Blöchl, *Phys. Rev. B* **50**, 17953 (1994).
- [38] G. Kresse and D. Joubert, *Phys. Rev. B* **59**, 1758 (1999).
- [39] J. P. Perdew, K. Burke, and M. Ernzerhof, *Phys. Rev. Lett.* **77**, 3865 (1996).
- [40] S. L. Dudarev, G. A. Botton, S. Y. Savrasov, C. J. Humphreys, and A. P. Sutton, *Phys. Rev. B* **57**, 1505 (1998).
- [41] S. Qiao, X. Li, N. Wang, W. Ruan, C. Ye, P. Cai, Z. Hao, H. Yao, X. Chen, J. Wu, Y. Wang, and Z. Liu, *Phys. Rev. X* **7**, 041054 (2017).
- [42] I. Lutsyk, K. Szalowski, P. Krukowski, P. Dabrowski, M. Rogala, W. Kozłowski, M. Le Ster, M. Piskorski, D. A. Kowalczyk, W. Rys, R. Dunal, A. Nadolska, K. Toczek, P. Przybysz, E. Lacińska, J. Binder, A. Wysmolek, N. Olszowska, J. J. Kolodziej, M. Gmitra, T. Hattori, Y. Kuwahara, G. Bian, T.-C. Chiang, and P. J. Kowalczyk, *Nano Res.* **16**, 11528 (2023).
- [43] P. Darancet, A. J. Millis, and C. A. Marianetti, *Phys. Rev. B* **90**, 045134 (2014).
- [44] H. Lin, W. Huang, K. Zhao, S. Qiao, Z. Liu, J. Wu, X. Chen, and S.-H. Ji, *Nano Res.* **13**, 133 (2020).
- [45] W. C.-W. Huang, S. Mu, G. von Witte, Y. S. Li, F. Kurtz, S.-H. Hung, H.-T. Jeng, K. Rossnagel, J. G. Horstmann, and C. Ropers, (2024), [arXiv:2405.20872](https://arxiv.org/abs/2405.20872) [cond-mat.mes-hall].
- [46] S. Grimme, J. Antony, S. Ehrlich, and H. Krieg, *J. Chem. Phys.* **132**, 154104 (2010).
- [47] B. Yang, X. Sun, X. Li, X. Jiang, M. Yan, B. Zhao, Z. Wang, S. Chen, H. Sun, X. Xing, W. Yi, X. Chen, Y. Zhang, and X. Liu, *J. Mater. Chem. C* **14**, 640 (2026).
- [48] I. Sánchez-Ramírez, M. G. Vergniory, and F. de Juan, *Phys. Rev. B* **110**, 195138 (2024).
- [49] Z. Wang, Y.-Y. Sun, I. Abdelwahab, L. Cao, W. Yu, H. Ju, J. Zhu, W. Fu, L. Chu, H. Xu, and K. P. Loh, *ACS Nano* **12**, 12619 (2018).
- [50] X. Jiang, T. Yilmaz, E. Vescovo, and D. Lu, *Phys. Rev. B* **109**, 115112 (2024).
- [51] S. Barja, S. Refaely-Abramson, B. Schuler, D. Y. Qiu, A. Pulkin, S. Wickenburg, H. Ryu, M. M. Ugeda,

C. Kastl, C. Chen, C. Hwang, A. Schwartzberg, S. Aloni, S.-K. Mo, D. Frank Ogletree, M. F. Crommie, O. V.

Yazyev, S. G. Louie, J. B. Neaton, and A. Weber-Bargioni, [Nat. Commun.](#) **10**, 3382 (2019).